In-situ deposition of oxidized porous metal nanoparticles on the surface of picosecond laser-induced micro/nano structures

Chemical Engineering Journal 460 (2023) 141582

Contents lists available at ScienceDirect

Chemical Engineering Journal

journal homepage: www.elsevier.com/locate/cej

In-situ deposition of oxidized porous metal nanoparticles on the surface of picosecond laser-induced micro/nano structures: A new kind of meta-surface equipped with both super-hydrophobicity and anti-reflectivity

Aifei Pan [a,b], Xuesong Mei [a,b,*], Wenjun Wang [a,b,*], Yong Xia [a], Ya-Qiong Su [c,d], Sikai Zhao [e], Tong Chen [f]

[a] State Key Laboratory for Manufacturing System Engineering, Xi'an Jiaotong University, Xi'an 710054, China
[b] Shaanxi Key Laboratory of Intelligent Robots, Xi'an 710054, China
[c] School of Chemistry, Xi'an Key Laboratory of Sustainable Energy Materials Chemistry, State Key Laboratory of Electrical Insulation and Power Equipment, Xi'an Jiaotong University, Xi'an 710049, China
[d] Laboratory of Inorganic Materials & Catalysis, Schuit Institute of Catalysis, Eindhoven University of Technology, P.O. Box 513, 5600 MB Eindhoven, The Netherlands
[e] School of Resources and Civil Engineering, Northeastern University, Shenyang 110819, China
[f] Air and Missile Defense College, Air Force Engineering University, Xi'an 710051, China

ARTICLE INFO

Keywords:
Picosecond laser
Porous nanostructure
In-situ deposition
Broadband anti-reflectivity
Super-hydrophobicity

ABSTRACT

This paper proposes a new kind of composite micro/nano structure composed of porous nanomaterials including titanium (Ti) gradient material and titania (TiO_2) gradient material. The composite structure is fabricated via in-situ deposition of gradiently distributed and oxidized porous titanium nanoparticles on the surface of picosecond laser-induced micro/nano structures. The porous composite layer made up of Ti gradient material and TiO_2 gradient material shows the best anti-reflectivity. The ability of TiO_2 for absorbing $-CH_3$ hydrophobic group and the air cushion effect of nanostructure endow the TiO_2 gradient porous material with hydrophobic characteristics. Then, the period and height of the desired microstructure of the composite micro/nano structure with the best super-hydrophobicity and anti-reflectivity are confirmed to be about 10 μm and more than 10 μm, respectively. The designed composite micro/nano structures are fabricated using picosecond laser induction processing strategy with the etched depth of the materials being only about 12 μm. The reflectance of the designed composite micro/nano structure is around 2 % from the visible band to the near-infrared band and below 20 % from the ultraviolet to middle-infrared band. Moreover, its slip angle is just 4° and contact angle 167.

1. Introduction

As an emerging technology for surface engineering, micro/nano structure manufacturing has a huge application prospect in aerospace, microelectronics, biomaterials, automotive and energy and other technical fields. In particular, biomimetic antireflective surfaces with micro/nano structures have drawn increasing attention owing to their promising and wide applications, such as photovoltaic industry [1,2], broadband thermal sources [3,4], and optical sensors [5,6]. Considering surface with a single function has poor work performance, adaptability and life span, multi-functional surface is an inevitable trend in the development of micro/nano surface manufacturing. In practice, objects with antireflective surface are mostly operated in harsh environments, including dusty, humid, rainy, and snowy days, which requires surface functions more than antireflection. It is well known that the super-hydrophobic surface can further contribute to other properties [7], such as anti-icing [8,9], anti-corrosion [10,11], self-cleaning [12,13], anti-drag [14] and electrocatalytic activity [15]. In this context, a kind of micro/nano-structure which simultaneously has functions of both super-hydrophobicity and anti-reflectivity would not only improve the working performance of the device but would also allow it to serve in adverse working conditions [16–19]. Now, the balanced design and fabrication method of multifunctional surface has become the hot and difficult issue of scientific research.

To design such a bi-functional surface texture, the desired micro/nano-structure should satisfy the structure commonality for different functions. On the one hand, the function of microstructure is to increase the specific surface area. In detail, microstructures can enable gas to be

* Corresponding authors at: State Key Laboratory for Manufacturing System Engineering, Xi'an Jiaotong University, Xi'an 710054, China.
E-mail addresses: xsmei@mail.xjtu.edu.cn (X. Mei), wenjunwang@mail.xjtu.edu.cn (W. Wang).

https://doi.org/10.1016/j.cej.2023.141582
Received 1 October 2022; Received in revised form 13 January 2023; Accepted 25 January 2023
Available online 2 February 2023

stored between the water drop and substrate to maintain the surface super-hydrophobicity and increase the number of refractions (Fig. 1a) to reduce surface reflectance [20], respectively. In general, high-aspect-ratio microstructures can be beneficial for both super-hydrophobicity [21] and anti-reflectivity [22]. Considering that the mechanical strengths of the surface with high-aspect-ratio microstructures are poor, the working performance of nanostructures should be enhanced under the condition of a low aspect ratio to meet the strength requirement. On the other hand, the function of nanostructure is different. In terms of super-hydrophobicity, nanostructure works as an air cushion to Cassie-Baxter state of the surface, where the pore interconnection should be enough for gas storage [23,24]. Some studies have demonstrated that porous nanostructures have better mechanical stability and their internal large specific surface area is beneficial for super-hydrophobicity [23]. In terms of reducing reflectivity, nanostructure works as lamella with a gradient refractive index [25] (Fig. 1b), so that the material concentration gradually decreases away from the substrate [26]. Therefore, porous nanostructures with gradient material concentration are suitable both for anti-reflectivity and super-hydrophobicity.

Indeed, a desired functional micro/nano structure should be specific to material behavior, especially for the anti-reflectivity of metal. With high complex refractive index, metals typically have high reflectivity from the visible to the infrared band. In addition, metal nanostructures can only introduce a narrow band of low reflection around resonance absorption [27]. Even though the gradient refractive index is an effective way to reduce surface reflectance, it is infeasible for metal nanostructures because their skin depth is only a few dozen nanometers. It is well known that metal exposed to air inevitably goes through oxidization, and metallic oxide has an optical skin depth in the micrometer or even millimeter scale. A reasonable configuration of metallic oxide nanostructures can lead to a gradient refractive index on the surface of a metal, that is, the concentration of metallic oxide nanostructures gradually drops with the distance from the surface [28]. Nevertheless, the metallic oxide cannot absorb light in the visible and near-infrared regions. Moreover, there is a difference in complex permittivity between the metal and metallic oxide, causing unsatisfactory anti-reflective performance. For these reasons, the property of the metal oxide material near the metal substrate should be similar to that of metal to serve as a lamella with a gradient refractive index. Therefore, a processing strategy of adjusting the chemical composition together with surface texturization is necessary for the fabrication of materials with anti-reflective properties.

Additionally, a super-hydrophobic surface is characterized by contact angle larger than 150° [29] and slip angle smaller than 10° [30]. Regarding the super-hydrophobicity of the micro/nano structures, the inherent hydrophobic property of the material is extremely important. So far, surface chemical modification of materials to obtain low surface energy, such as introduction of $–CH_3$ and $–CF_3$ groups, is a common method to achieve a super-hydrophobic surface [31]. Recently, it has been verified that metal oxides are inclined to absorb organics and show hydrophobic properties, such as ZnO [32], TiO_2 [33], etc. Hence, metallic oxide nanoparticles would not only help with low reflectance but would also provide super-hydrophobicity.

There is a strong need to develop methods for fabricating high-aspect-ratio round-top microstructures with porous nanostructures which have a gradient oxidization. Laser processing, with the characteristics of flexibility and elaborate material removal, has been demonstrated as a novel approach for surface texturization [34]. Much attention has been given to laser structuring combined with other post-processing methods for oxidization [35,36], where the characteristics of gradient oxidization are out of reach. Actually, in the process of ultrashort pulsed laser ablation, nanoscale vaporized particles can be obliquely deposited in the area close to the ablation zone to form porous nanostructures [37], where the nanostructures are not aggregated into microscale film due to the low temperature of the microstructure. In addition, radicals in air or on the surface of material were produced and photochemical reaction occurred in the laser irradiation, which will change the surface material properties [38,39]. The oxidization degree of metal has a positive relationship with the flight time for deposition, where the nanoparticles with less oxidization fall first to form the gradient oxidized material. The pre-deposition oxides can be removed during the processing of laser-induced microstructure because the

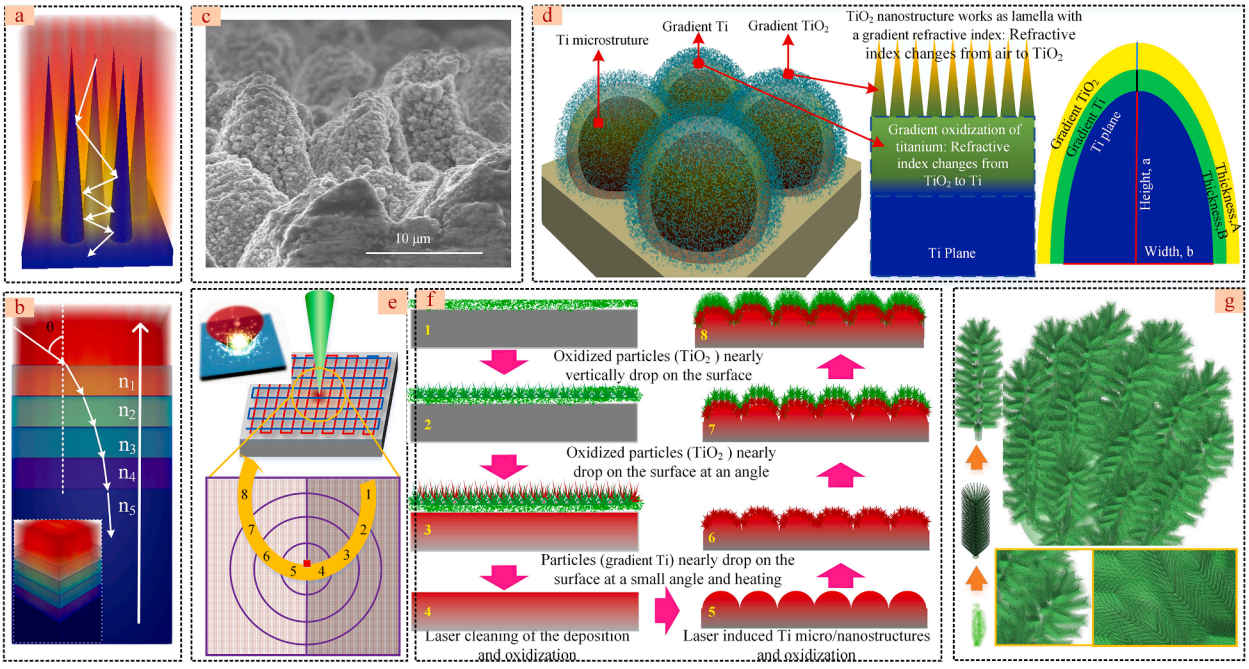

Fig. 1. (a, b) Schematic diagram of the gradient refractive index of nanostructure and the role of microstructure in the reduction of surface reflectance. (c, d) Scanning Electron Microscope (SEM) image and structure diagram of the proposed composite micro/nano structures. (e, f) Preparation procedure of the composite micro/nano structures with picosecond pulses, where the red and green colors represent the gradient Ti and gradient TiO_2, respectively. (g) Structure diagram of TiO_2 gradient material. (For interpretation of the references to color in this figure legend, the reader is referred to the web version of this article.)

ablation threshold of a metallic oxide is lower than that of metal. In this regard, a simple ultrashort laser scanning method can be used to produce metal micro/nano structures covered with metallic oxide of graded refractive index. Apart from shaping microstructure surface into round-top, our previous study showed that such oblique deposition also results in preferential deposition of materials on the top of the microstructures, which increases the depth of microstructure [40].

In this paper, a new kind of micro/nano structure with porous nanostructures of gradient oxidization on the surface of titanium (named the composite micro/nano structure) was proposed. As shown in Fig. 1 c and d, the surface of the microstructure was covered with the Ti gradient material (refractive index changes from TiO_2 to titanium) and TiO_2 gradient material (refractive index changes from air to TiO_2). Furthermore, this paper also proposed one-step high-repetition-rate picosecond laser ablation accompanied by in-situ inverse laser deposition in air to fabricate the composite micro/nano structure, as shown in Fig. 1e. For the zone marked with a red point in Fig. 1e, the formation procedure of the composite micro/nano structure is shown in Fig. 1f, as the laser beam moves from area "1″ to area "8". As shown in Fig. 1g, based on the in-situ inverse laser deposition, the TiO_2 gradient material consists of the gradient distributed porous TiO_2 nanoparticles. To obtain the composite micro/nano structure mentioned above, this paper performed an in-depth analysis of the following four aspects:

(1) Does the composite film with a combination of Ti gradient and TiO_2 gradient film show the best anti-reflectivity?

(2) How does the TiO_2 gradient film show super-hydrophobicity?

(3) Which microstructure is suitable for the dual anti-reflective and super-hydrophobic micro/nano structure?

(4) What is the ultrashort laser processing scheme and how to fabricate the composite micro/nano structures?

2. Results and discussion

2.1. Anti-reflectivity and super-hydrophobicity of the composite film with a combination of Ti gradient and TiO_2 gradient materials

2.1.1. Broadband anti-reflection ability of the composite film based on gradient refraction effect

The reflectance in the interface between two media can be computed via $R = \left[(n_2 - n_1)^2 + (k_2 - k_1)^2\right] \Big/ \left[(n_2 + n_1)^2 + (k_2 + k_1)^2\right]$ when the light beam propagates from medium "1″ to medium "2", where the n_i and k_i are the real part and imaginary part of the refractive index of the medium, respectively, and i is the medium number. In this regard, reducing the difference between the refractive indices of the two media is an effective method to decrease the surface reflectance, which is called as gradient refraction effect [41].

First, the neglible impact of the size effect of TiO_2 nanoparticles on their optical property and the feasibility of the gradient oxidization of titanium contributing to the gradient refractive index were verified (see Fig. S1 and Fig. S2). Then, a new kind of lamella with a composite gradient refractive index was proposed herein, where the gradient distribution of TiO_2 nanoparticles forms the first layer and the gradient oxidization of titanium forms the lower layer. Four kinds of layers with a total thickness of 1 μm were chosen to theoretically verify the anti-reflectivity of the composite layer. The typical films and their corresponding reflectance are shown in Fig. 2 a and b. The type A, B, C, and D lamellas are TiO_2 film, TiO_2 gradient film, Ti gradient film, and the composite film with the gradient refractive index, respectively. Considering that a gradiently oxidized film is formed in the process of metal oxidization, a 50-nm thick film was added and the refractive index was changed from TiO_2 to titanium to form the type A and B films. TiO_2

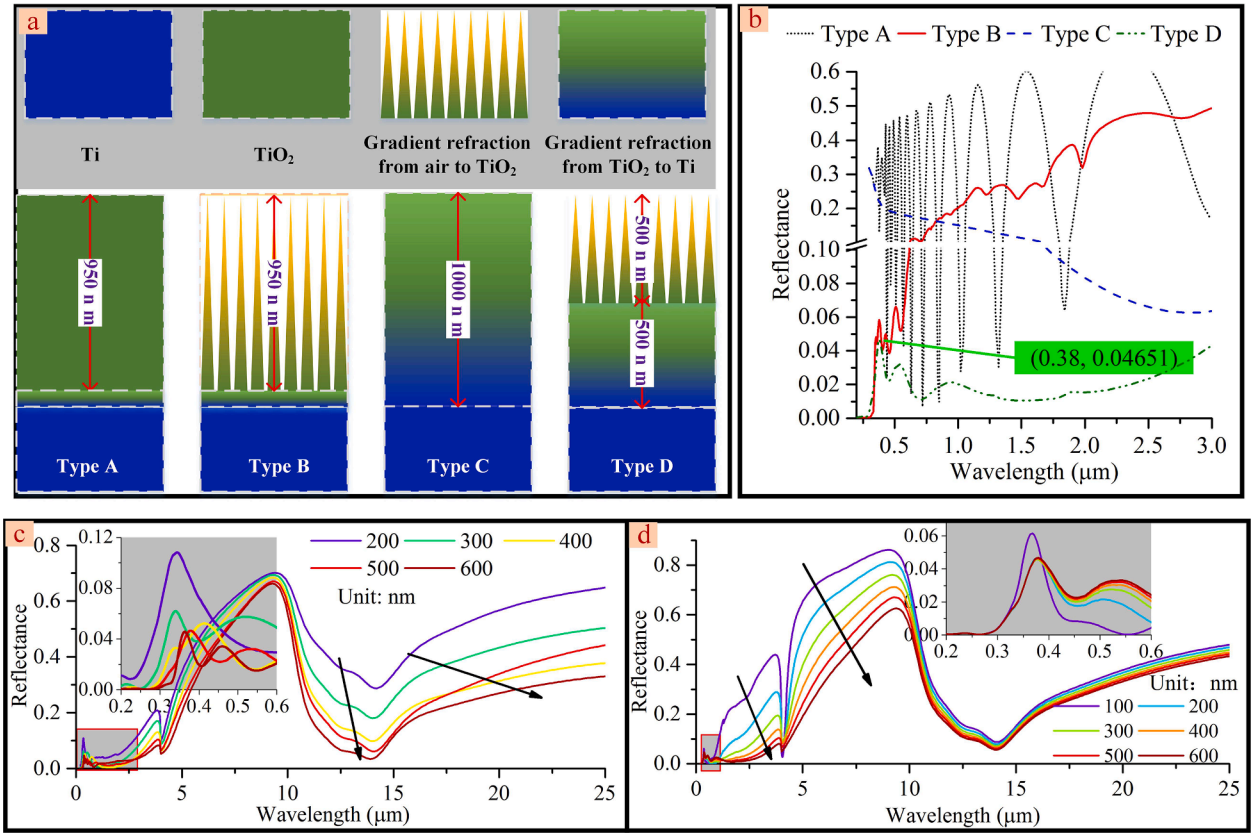

Fig. 2. (a, b) Four kinds of films and the corresponding reflectance. (c) Change in reflectance of the sample with the thickness of gradient refractive TiO_2 (the thickness of gradiently-oxidized titanium film is 500 nm). (d) Change in reflectance of the sample with the thickness of gradient refractive TiO_2 (the thickness of gradiently-distributed TiO_2 film is 500 nm).

film (type A) shows a fluctuant and high reflectance in the waveband from 300 nm to 3 μm. Additionally, the reflectance of the TiO_2 gradient film (type B) is low in the waveband below 400 nm and then gradually increases with light wavelength. In contrast, the reflectance of the Ti gradient film (type C) decreases with light wavelength, while the composite film with the gradient refractive index (type D) exhibits the lowest reflectance.

Then, the influence of the specific working waveband of two layers on the anti-reflective performance of the type D film was investigated. As shown in Fig. 2c, the variation of the reflectance of the sample with increase in the thickness of TiO_2 gradient film is mainly divided into three regions. First, the reflectance of the sample decreases slightly and then fluctuates in the waveband less than 500 nm. The reflectance of the sample decreases slightly in the waveband less than 10 μm. Finally, when the incident wavelength is larger than 10 μm, there is chemical bond resonance absorption in the TiO_2 material, so that the reflectance of the sample decreases obviously. The role of Ti gradient film on broadband anti-reflectivity was also analyzed with the increase in its film thickness, as shown in Fig. 2d. When the incident wavelength is less than 500 nm, the high reflection point slightly increases and moves to higher wavelengths, and the decline rate on the right side of the reflectance peak becomes smaller. The reflectance of the material decreases gradually with the incident wavelength from the visible spectrum to the spectrum with the wavelength of 10 μm and remains almost the same at incident wavelengths larger than 10 μm.

It can be concluded that the function range of Ti gradient film is mainly in the waveband with light wavelength of less than 10 μm, while that of TiO_2 gradient film is mainly in the waveband with light wavelength of more than 10 μm. In this context, the combination of the two layers can achieve low reflectance in the whole band. Additionally, the reflectance of the composite film is relatively high in the wavelength range from 5 μm to 10 μm, where the microstructure can be applied to further reduce its reflectance.

2.1.2. Super-hydrophobic ability of TiO_2 gradient material combined with absorbed hydrophobic group and air cushion effect

Surface wetting of the sample is attributed to the top layer, namely the TiO_2 gradient material. Hence, the effects of surface defects and nanostructure of the TiO_2 gradient material on its hydrophobicity were investigated. As shown in Fig. 3a, the absorption energies of H_2O for the –OH and $–CH_3$ groups on the surface of TiO_2 are −0.25 eV and −0.06 eV, respectively. As a result, the $–CH_3$ group shows hydrophobicity, and the –OH group shows hydrophilicity. Generally, TiO_2 has a polar Ti-O bond and the absorbed H_2O molecule goes through a dissociation reaction to form a hydrophilic group (–OH) on the surface of TiO_2 [42]. Hence, the surface of titanium shows super-hydrophilicity after laser processing. However, volatile organic compounds in the air are adsorbed on TiO_2 to form hydrophobic groups ($–CH_3$, $–CH_2$, etc.) [43].

Furthermore, the "cool" processing characteristic of the ultrashort laser allows the generation of oxygen vacancies on TiO_2 [44]. Oxygen vacancy defects make Ti atoms directly exposed to the outside, and Ti can easily combine with O atoms rather than H atoms. That is, it is easier to combine with hydrophilic groups and leave hydrophobic groups outside, which finally form a hydrophobic surface. It is well known that ethanol molecules have both hydrophobic group ($–CH_3$) and hydrophilic group (–OH). As shown in Fig. 3b, type 1 is the normal rutile phase TiO_2 (0 0 1) lattice plane, type 2 is formed by removing the top layer of oxygen based on type 1, and type 3 is formed by removing two oxygen atoms in the middle based on type 2. Canonical ensemble (NVT ensemble) was performed at the temperature of 300 K after geometry optimization. It can be seen that when the –OH group of ethanol is close to the surface, ethanol goes through a dissociation reaction, and the –OH group remains on the surface of type 1 and shows hydrophilicity. However, for type 2 and type 3, the –OH group of ethanol forms a bond with TiO_2, while the $–CH_3$ group is outside and shows hydrophobicity.

Then, as shown in Fig. 3c, Lennard-Jones potential was applied to fit the potential energy between the O atom and $–CH_3$ adsorbed by TiO_2,

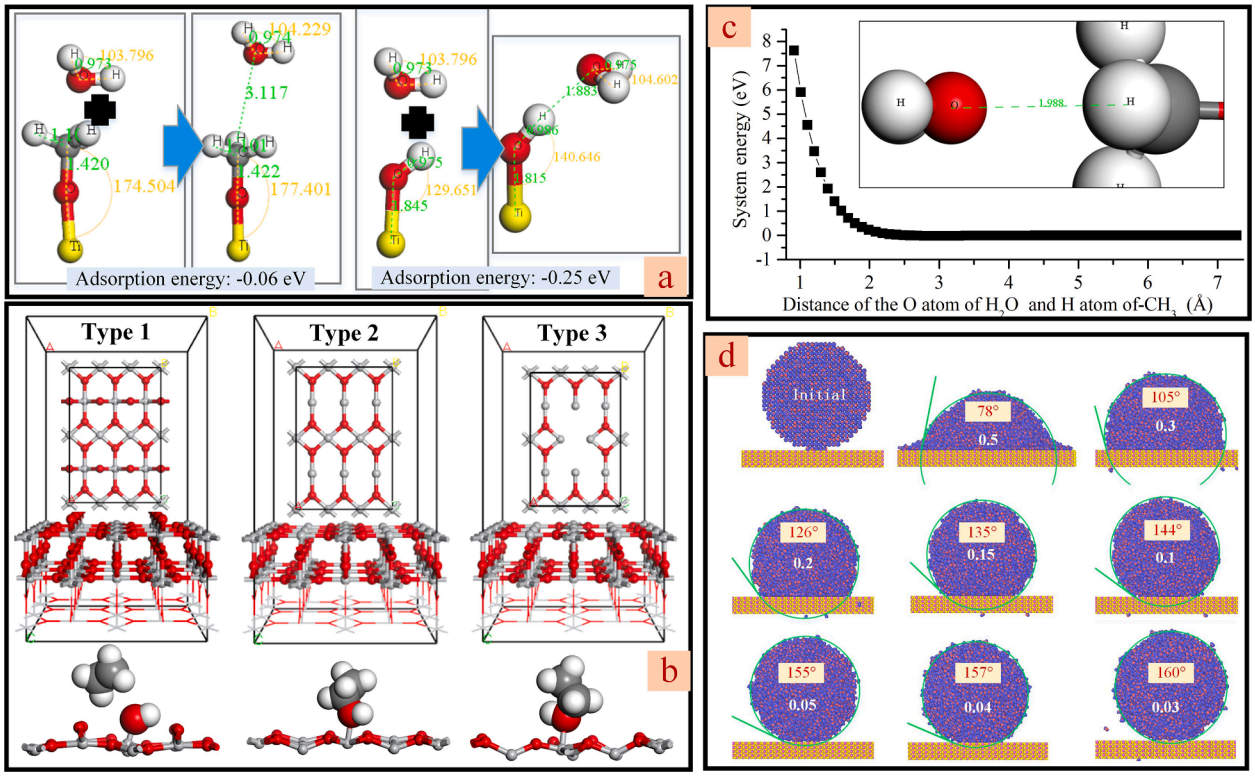

Fig. 3. (a) Effect of $–CH_3$ and –OH groups on the adsorption of H_2O molecule. (b) Role of oxygen vacancy on the adsorption and dissociation reaction of ethanol. (c) Energy potential between the H_2O molecule with $–CH_3$ adsorbed on the surface of TiO_2. (d) Contact angle of a droplet on the surface with various energy constants of Lennard-Jones potential.

which takes the form:$E = 4\varepsilon\left[(\sigma/r)^{12} - (\sigma/r)^{6}\right] r < r_c$, where ε is the energy constant of 0.022 eV (0.6 kcal/mol), σ is the distance constant of 2.65 Å, r is the distance between two atoms, and r_c is the cutoff distance which is 10 Å here. Accordingly, the hydrophobicity of the materials increases with the decrease in value of ε.

Furthermore, the nanostructure is responsible for the air cushion effect to make the surface hydrophobic, which can be represented by the energy constant. It can be seen from Fig. 3d that the surface with only $-CH_3$ hydrophobic group (ε is equal to 0.6 kcal/mol) is not super-hydrophobic, and the contact angle increases with the decrease in energy constant. Therefore, the combination of the hydrophobic group and the air cushion effect of nanostructure makes the surface super-hydrophobic.

2.1.3. *Experimental verification of the super-hydrophobicity and anti-reflectivity of the composite film*

Nanosecond laser processing was selected to make full use of the deposition of ablated particles and their thermal oxidization to prepare the composite film on the surface of titanium first [45]. As shown in Fig. 4 a1-a3, samples A, B, and C refer to the oxidized surface that is not covered, partly covered and completely covered with the porous TiO_2 nanostructure, respectively.

The theoretical X-ray diffraction (XRD) results of the composite layer are shown in Fig. 4 b1. Red, blue, and green lines are the XRD patterns of pure titanium, Ti gradient material, and TiO_2, respectively. Peaks 1 and 4 are the XRD peaks of TiO_2, peak 2 is the XRD peak of pure titanium and Ti gradient material, peak 3 and peak 5 are XRD peaks of Ti gradient material and TiO_2, and peak 6 is the XRD peak of pure titanium in all the samples. Hence, the ratio of peak 1–5 to peak 6 was used to determine the contents of the Ti gradient material and TiO_2.

Experimental XRD patterns of the three samples are shown in Fig. 4 b2. By comparison with the peak highlighted by the orange dotted circles in Fig. 4 b1 and b2, the formation of the Ti gradient material can be demonstrated. To analyze the contents of Ti gradient material and TiO_2, the XRD patterns were baseline corrected, and the intensity ratios of peaks 1–5 to peak 6 were calculated, as shown in Fig. 4 b3. Peak 1–5 ratio rises with increase in the amount of porous TiO_2 nanostructure, which means that the content of both Ti gradient material and TiO_2 increases. Furthermore, the thermal action of nanosecond laser is

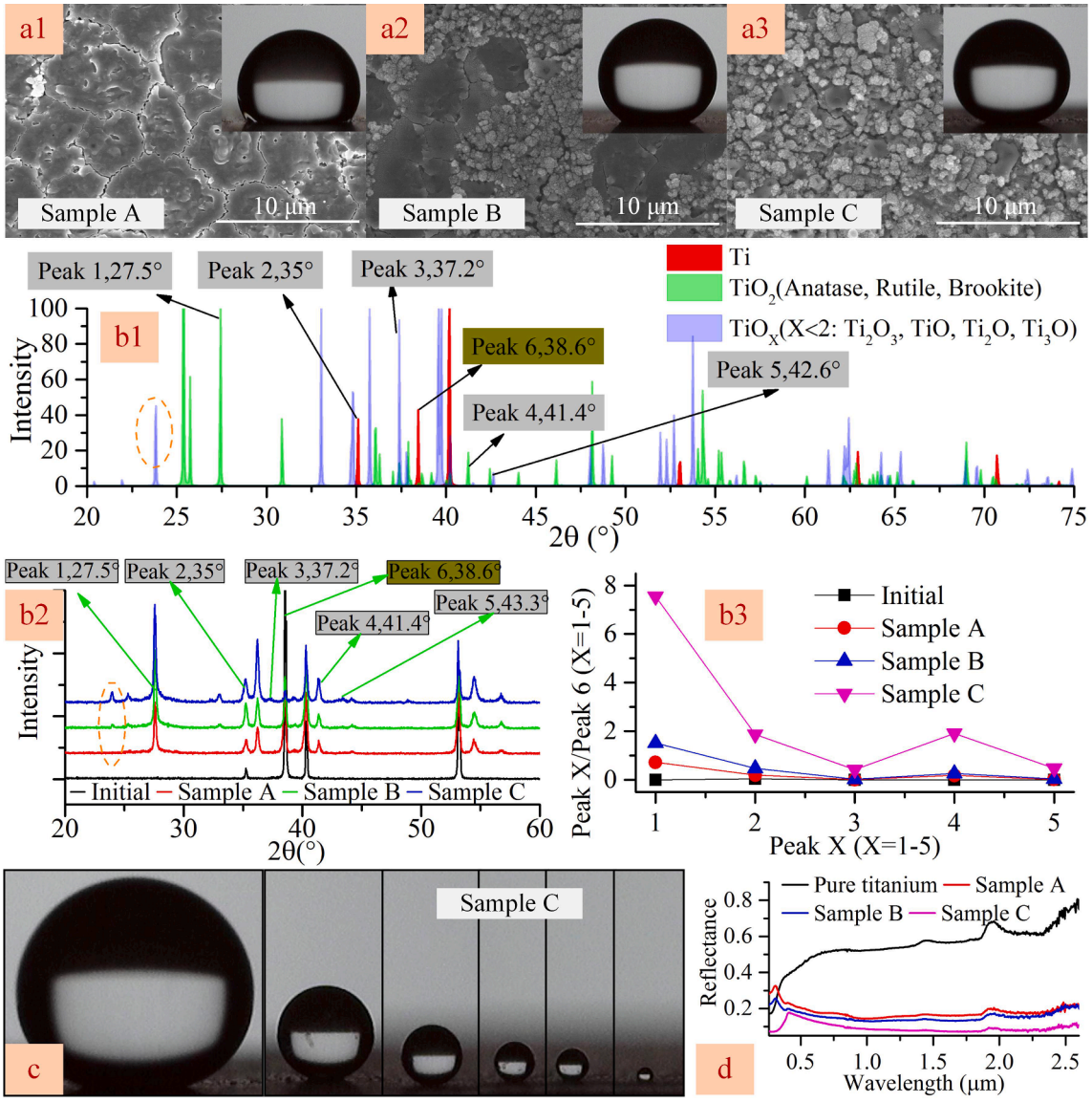

Fig. 4. (a1-a3) Samples of the oxidized surface not covered, partly covered, and completely covered with the porous TiO_2 nanostructure and their contact angle with a droplet (5 μL). (b1) Theoretical XRD patterns of pure titanium, Ti gradient material, and TiO_2. (b2, b3) Experimental XRD patterns of the three samples and the ratio of peaks 1–5 to peak 6. (c) Contact angle of sample C with various droplet sizes. (d) Reflectance of the three samples and the unmachined surface.

obvious. Therefore, the content of TiO_2 increases much more than that of Ti gradient material.

As shown in Fig. 4 a1-a3, the role of the air cushion effect is enhanced by increasing the coverage ratio of porous TiO_2 nanostructure, so that the contact angle of the samples increases (134°, 150°, and 163°). As shown in supplemental video1, sample B exhibits adherent hydrophobicity because the porous TiO_2 nanostructure is not completely covered on the oxidized surface. In addition, as shown in Fig. 4c, unlike conventional microstructure, the contact angle for sample C does not decrease with reduction in the size of the droplet. The reflectance of the three samples is shown in Fig. 4 d. The reflectance of samples decreases with increase in content of Ti gradient material and proportion of porous TiO_2 nanostructure, which is consistent with Fig. 2 a and b.

2.2. Size determination of microstructure in the composite micro/nano structure for anti-reflectance and super-hydrophobicity

2.2.1. Size determination of microstructure in the composite micro/nano structure for anti-reflectance

The size of microstructure in the composite micro/nano structure suitable for anti-reflectance was investigated first. From the above results, the reflectance of the composite film with TiO_2 gradient film and Ti gradient film in the waveband from 5 μm to 10 μm is relatively high, which can be decreased by applying the microstructure. As shown in Fig. S3, the period of the microstructure affects the position of the high reflectance (black dotted line) and the total reflectance decreases with increase in the height of the microstructure. Here, the thicknesses of Ti gradient material and TiO_2 were set as 500 nm and 1 μm, respectively. The whole height and period of pure microstructure and composite micro/nano structure were fixed as 14 μm and 10 μm, respectively. As shown in Fig. 5a, the reflectance of composite micro/nano structure is much lower than that of pure microstructure, especially from the visible to near-infrared band. As seen from the insets " f1, f2, and j", compared to the polished titanium, laser-induced microstructure (St1) with slight oxidization reduces the surface reflectance dramatically, but its reflectance at the infrared band increases up to 10 %. However, when the microstructure is covered with the deposited 2-μm thick metallic oxide film (St2), the reflectance at the visible spectrum is almost the same. However, reflectance decreases as the wavelength increases, where the slope of the reflectance to wavelength is lower to ensure lower reflectance at the middle-infrared band. With increase in the oxygen content, the optical property of the metallic oxide does not change strictly from that of metal to air. For example, when the incident wavelength is below 700 nm, the real part of the refractive index of titanium is smaller than

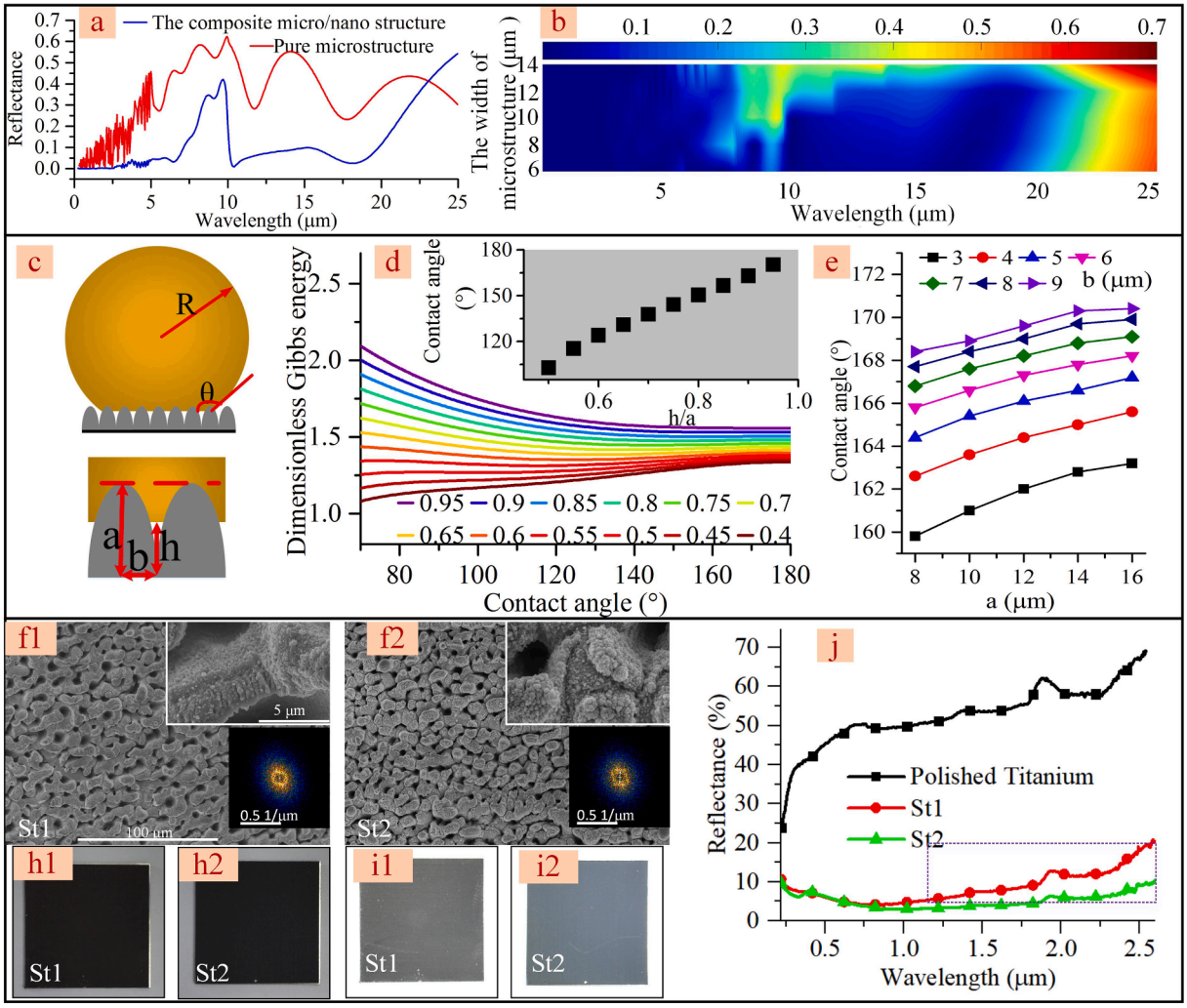

Fig. 5. (a) Comparison of the anti-reflectance of pure microstructure and composite micro/nano structure. (b) Reflectance of the composite micro/nano structure with various periods of the microstructure. (c) Contact section between the droplet and the microstructure. (d) Computation of the contact angle based on the dimensionless Gibbs energy. (e) Change in contact angle with the long and short axes of the ellipsoid at the *a*-*h* of 1 μm. (f1, f2, h1, h2, i1, i2) SEM images, photographs, and high-exposure photographs of pure microstructure and composite micro/nano structure. (j) Experimental reflectance of pure microstructure and composite micro/nano structure.

that of titania. This phenomenon can be verified by insets "h1, h2, i1, and i2". That is, the two samples show no difference in color, but with high light exposure, the surface covered with the metallic oxide shows a blue color (see insets d1, d2).

In addition, when the height of the composite micro/nano structure is fixed at 14 μm, its reflectance with variation of the period from 6 μm to 14 μm is shown in inset "b". When the period of composite micro/nano structure is larger than 10 μm, the reflectance in the waveband from 8 μm to 12 μm increases dramatically. As a result, the period of the microstructure should be less than 10 μm and a higher ablated depth is better.

2.2.2. Size determination of microstructure in the composite micro/nano structure for super-hydrophobicity

Next, the role of the microstructure of the composite micro/nano structure in super-hydrophobicity was investigated. According to the contact section between droplet and microstructure shown in Fig. 5c, the dimensionless Gibbs energy was obtained with Equation (1) (the details are given in the supplemental materials section), and the contact angle was computed when the minimum value of dimensionless Gibbs energy was reached.

$$G^* \equiv \frac{G}{\gamma_{LV}\pi^{1/3}(3V)^{2/3}} = F^{-2/3}\left\{\begin{array}{c} -\frac{3\sin^2\theta}{4ab}\left[a^2\left(\frac{\pi}{2}-\arcsin\frac{h}{a}\right)-h\sqrt{a^2-h^2}\right]\cos\theta_Y \\ +2(1-\cos\theta)+\sin^2\theta-\frac{3(a^2-h^2)}{4a^2} \end{array}\right\} \quad (1)$$

where V is the volume of the droplet, a and b are the long and short axes of the spheroid, respectively, h is the height that is not soaked with water, $F(\theta)$ is the volume transformation constant with the equation$F(\theta) = (2-\cos\theta+\cos^3\theta)$, and γ_{LV} is the interfacial energy between liquid and gas (72.75 mN/m).

When a is 8 μm and b is 2 μm, the contact angle increases with increase in h/a, which means that the air cushion effect is enhanced, as shown in Fig. 5d. The h value of the composite film should be in the submicron order. When a-h is fixed as 1 μm, the contact angle increases with increase in the values of a and b, and the increment of contact angle is less than 1° when b is larger than 6 μm, as shown in Fig. 5e. Thus, to ensure that the contact angle of the sample is larger than 165°, a and b should be larger than 10 μm and 5 μm, respectively.

In conclusion, the period of the microstructure suitable for anti-reflectance should be less than or equal to 10 μm and a greater height is better. In contrast, when a-h is equal to 1 μm, the period and height of microstructure suitable for super-hydrophobicity should be larger than 10 μm. Therefore, the period of microstructure should be ~ 10 μm, and its height should be greater than 10 μm.

2.3. Fabrication and performance evaluation of the composite micro/nano structures via picosecond pulses

Considering the period of microstructure around 10 μm, this paper proposed laser induction for one-step fabrication of the composite micro/nano structure, where the period and height of microstructure were restricted by laser power and scan speed rather than focused size. A preliminary selection of parameters for picosecond laser induction is shown in Fig. 4S.

2.3.1. Surface morphologies and crystal structure of the composite micro/nano structures

At the scan interval of 5 μm and scan mode of cross scanning, surface morphologies with various pulse energies and scan speeds are shown in Fig. 6a. It can be seen that the porous and oxidized nanostructure is covered on the surface of the microstructure. From the Fourier transform diagram, it can be seen that the average periods of microstructure are 8 μm, 10 μm, and 12 μm when the pulse energies are 4 μJ, 6 μJ, and 8 μJ. The number of overlapping spots is so high that the size of the microstructure does not change with scan speeds. In addition, the X-ray Photoelectron Spectroscopy (XPS) shown in Fig. S5 indicates the existence of TiO_2, oxygen vacancies, surface adsorbents of organic compounds on the surface of the composite micro/nano structures.

The mean height of the composite micro/nano structures with various pulse energies and scan speeds is shown in Fig. 6b. It can be seen that the mean height of the composite micro/nano structure increases with increase in pulse energy. In detail, for the pulse energies of 4 μJ and

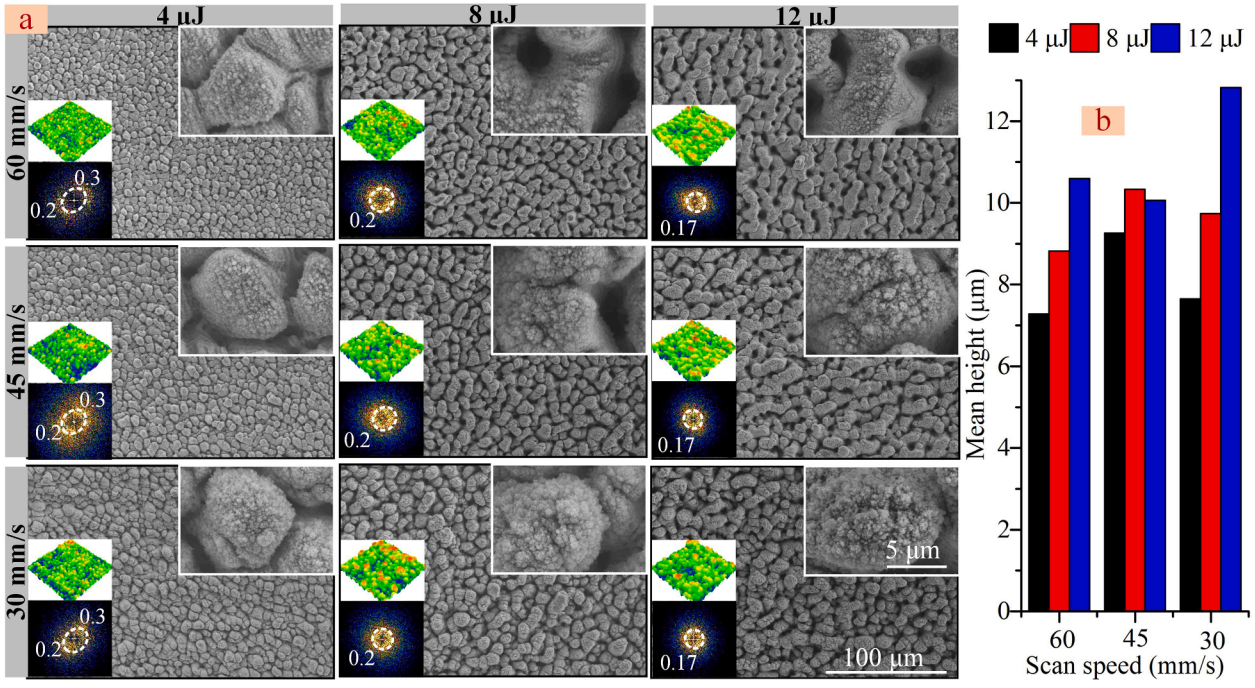

Fig. 6. (a) Surface morphologies and (b) mean height of the composite micro/nano structures at various pulse energies and scan speeds.

8 μJ, the mean height of the composite micro/nano structure reaches a maximum at the scan speed of 45 mm/s. For the pulse energy of 12 μJ, the mean height of the composite micro/nano structure at the scan speed of 30 mm/s is the highest. Therefore, even though the surface micro-melting is more obvious at the pulse energy of 12 μJ and low scan speed, the deposition of material on the surface of the microstructure at low scan speed increases the height of the microstructure.

As a result, based on only the period and height of the microstructure, the sample obtained at a pulse energy of 8 μJ and a scan speed of 45 mm/s shows the best anti-reflectivity, while the sample obtained with pulse energy of 12 μJ and scan speed of 30 mm/s shows the best super-hydrophobicity. However, it is also necessary to consider the amount of the Ti gradient materials and TiO_2 gradient materials and their role in the anti-reflectivity and super-hydrophobicity.

XRD analysis of the above mentioned samples was conducted to investigate the optimal amounts of Ti gradient material and TiO_2 gradient material, and the results are shown in Fig. 7a. After removing the bottom noise of XRD data, the ratio of the peaks 1–5 to peak 6 is shown in Fig. 7b. As shown in Fig. 4b1, peak 2 is the XRD peak of pure titanium and Ti gradient material, and peak 3 and peak 5 are XRD peaks of Ti gradient material and TiO_2. It can be seen from the ratio of peaks 1 and 4 (the XRD peaks of TiO_2), that the amount of the crystal phase of TiO_2 is very low compared to the Ti gradient material. In addition, the variation tendency of the ratio of peaks 2, 3, and 5 at various pulse energies and scan speeds is almost the same, which verifies that these peak ratios can indicate the amount of the Ti gradient material. It can be seen that the amount of Ti gradient material increases with increase in pulse energy. Furthermore, at the pulse energy of 8 μJ, the amount of Ti gradient material increases with decrease in the scan speed, but the variation tendency at the pulse energy of 12 μJ is the opposite. Then, the crystallinity of the samples can be computed via the proportion of background noise in XRD, where the amorphous material is the TiO_2 nanoclusters. As shown in inset "c", with the pulse energies of 4 μJ and 12 μJ, the amount of amorphous TiO_2 increases with decrease in the scan speed, while the variation tendency at the pulse energy of 8 μJ is the opposite.

In conclusion, for the pulse energies of 8 μJ and 12 μJ, the amount of the Ti gradient material increases while the amount of the TiO_2 gradient material decreases. Therefore, the amounts of the Ti gradient material and TiO_2 gradient material cannot increase simultaneously. From the size of the microstructure and the amount of composite layer with the gradient refractive index, it can be inferred that the sample with a pulse energy of 12 μJ and a scan speed of 30 mm/s has the best anti-reflectance and super-hydrophobicity.

2.3.2. *anti-reflectance of the composite micro/nano structures*

The reflectance of the above samples is shown in Fig. 8. For all the samples, the reflectance in the blue waveband increases with decrease in scan speed because the wavelength of 380 nm corresponds to the band gap of TiO_2 which has a high reflectance. In addition, when the pulse energy is 4 μJ, the slope of the reflectance to wavelength decreases from 4.77 to 2.61 with decrease in the scan speed, and the lowest reflectance at the scan speed of 30 mm/s is about 2 %. The deposition of materials increases at the pulse energy of 8 μJ, while the slope of the reflectance to

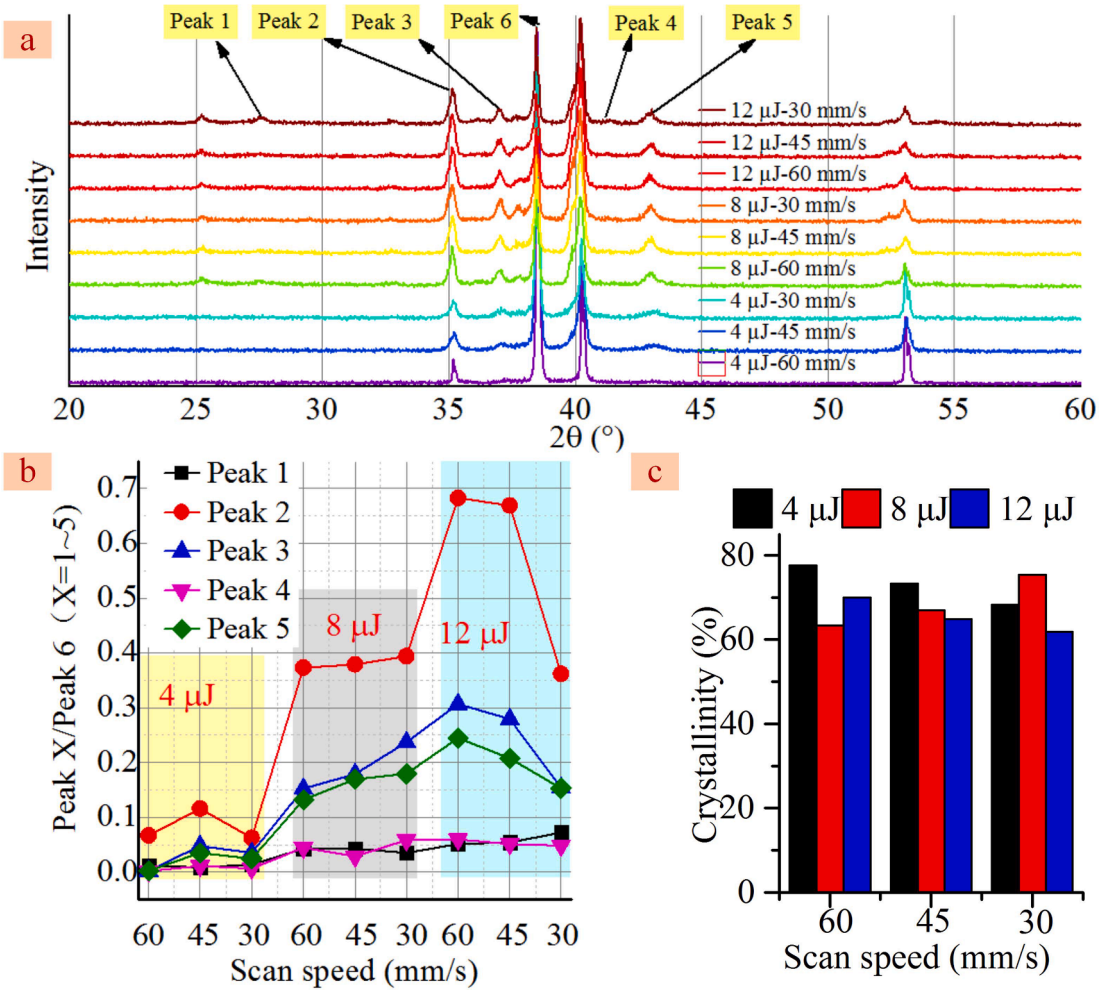

Fig. 7. (a) Experimental XRD patterns, (b) XRD peak ratios, and (c) crystallinity of the composite micro/nano structures with various pulse energies and scan speeds.

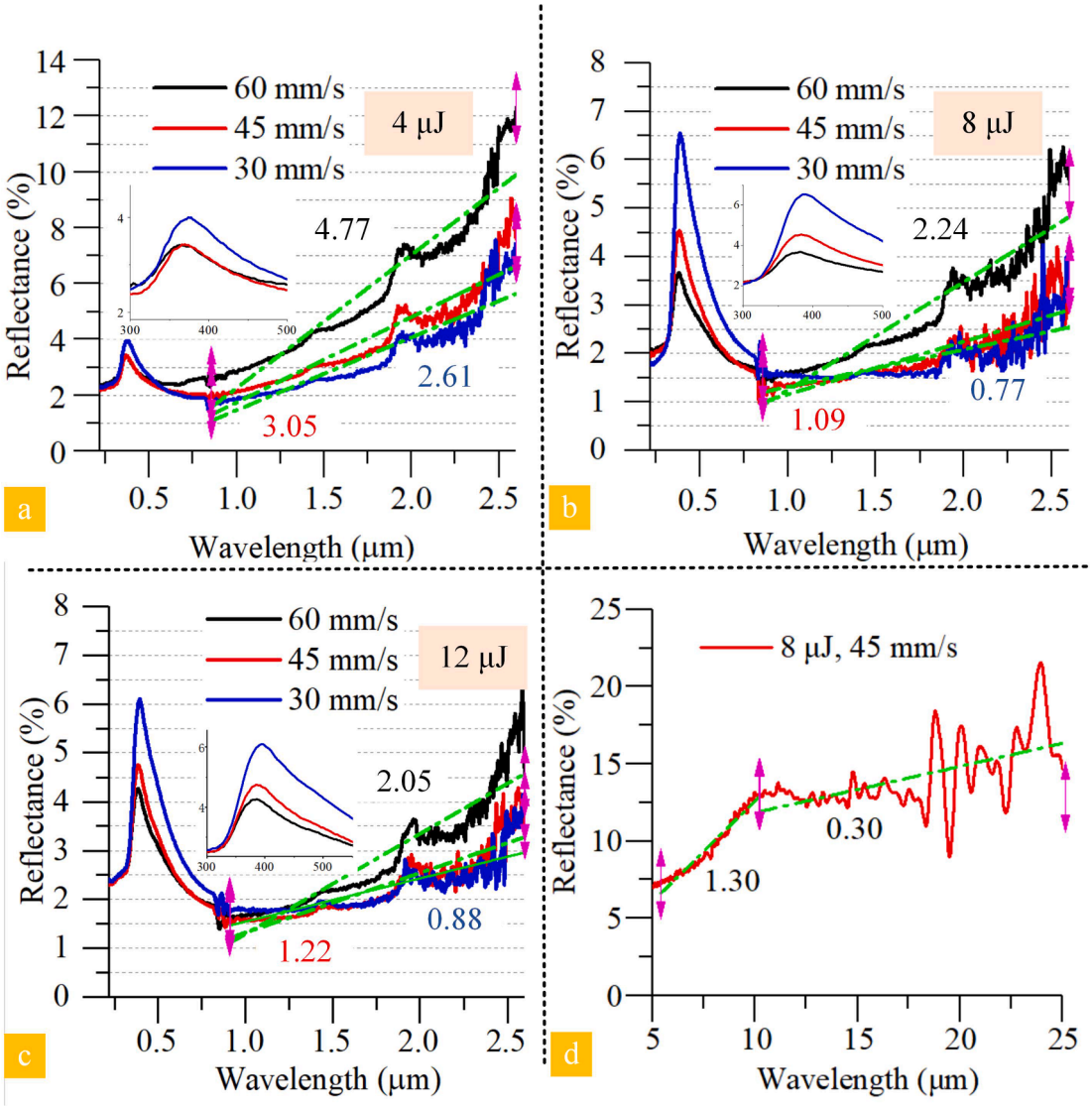

Fig. 8. Reflectance of samples obtained at various pulse energies and scan speeds.

wavelength decreases from 2.24 to 0.77 with decrease in the scan speed. The lowest reflectance at the scan speed of 30 mm/s is about 1.5 % and the near-infrared reflectance is below 3 %. The reflectance of samples obtained at the pulse energy of 12 μJ is almost the same as that at the pulse energy of 8 μJ.

Considering that the deposition of sample at the pulse energy of 4 μJ is not significant, it can be deduced that its anti-reflectivity is not good. In contrast, the reflectance values of the sample at the pulse energies of 8 μJ and 12 μJ and the scan speeds of 45 mm/s and 30 mm/s are almost the same. Here, the reflectance in the middle-infrared band of the sample obtained at the scan speed of 45 mm/s and pulse energy of 8 μJ was detected, as shown in Fig. 8d. It can be seen that the slope of the reflectance to wavelength in the waveband from 5 μm to 10 μm is 1.3, which is close to the slope in the near-infrared band of 1.09. Therefore, the slope of the reflectance to wavelength in the near-infrared band of the sample can be used to predict its reflectance in the middle-infrared band. Additionally, the reflectance is almost constant at wavelengths above 10 μm.

Therefore, the reflectance of the sample is below 20 % from the ultraviolet to mid-infrared band, indicating that the composite micro/nano structure helped realize the broadband anti-reflectance property of metal. According to the amount of deposition, the height of microstructure, and the reflectance in the visible and near-infrared wavebands, it can be deduced that the samples obtained at the scan speed of 30 mm/s and pulse energy of 12 μJ and 8 μJ have the best anti-reflectance.

2.3.3. *Super-hydrophobicity of the composite micro/nano structures*

The contact angle of all samples is above 160° and shows little difference, as depicted in Fig. 9b. Additionally, the slide angle of all samples is shown in Fig. 9c. All the slide angles of samples are below 10° at the pulse energy of 12 μJ, which indicates that these samples exhibit super-hydrophobicity, without any additional chemical modification. Specifically, the slide angle of sample IV drops down to 4° as the scan speed decreases to 30 mm/s. In contrast, at the pulse energy of 8 μJ, the slide angle increases as scan speed decreases. Moreover, when the pulse energy drops down to 4 μJ, only sample II shows non-adhesive hydrophobicity with a slide angle of 27°. In addition, as shown in Fig. 9a, the contact angles between the droplet and sample IV with various droplet sizes are almost the same and also show super-hydrophobicity. In this condition, it can be predicted that the broken small droplet would not remain on the surface of the sample during the spreading and spattering of the droplet upon contact with the surface of the sample.

It is well known that both the microstructure and porous nanostructures affect the wetting property of the samples. For the pulse energies of 8 μJ and 12 μJ, the slide angle has a negative relationship with

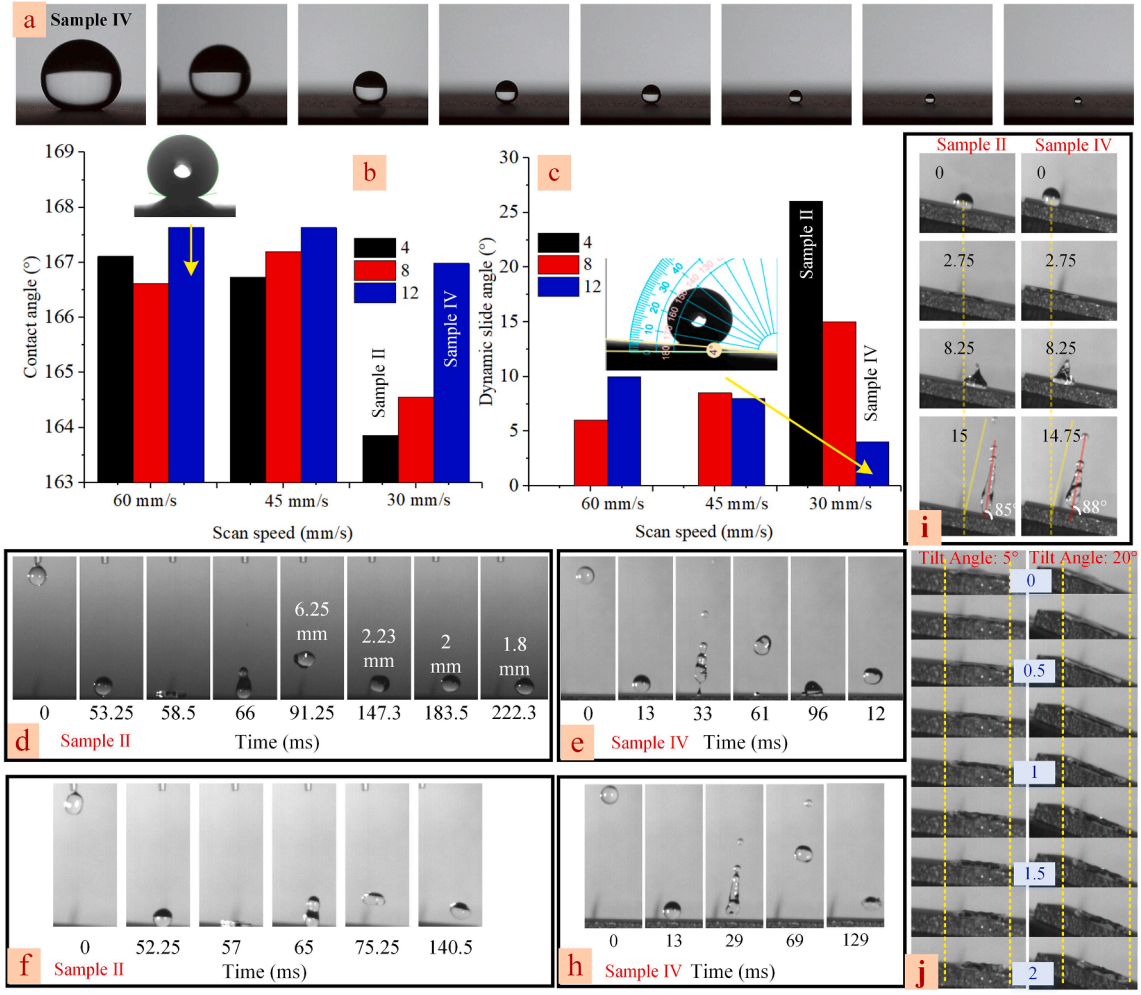

Fig. 9. (a) Contact angles between the droplet and sample IV with various droplet sizes. (b, c) Contact angle and slide angle of the droplet with the samples with various pulse energies and scan speeds. (d, f) Bouncing dynamics of droplets falling from the height of 2 cm and 10 cm onto sample II, respectively. (e, h) Bouncing dynamics of droplets falling from the height of 2 cm and 10 cm onto sample IV, respectively. (i) Bouncing dynamics of droplets falling from the height of 10 cm onto samples II and IV with a tilt angle of 10°. (i) Bouncing dynamics of droplets falling from the height of 10 cm onto sample IV with tilt angles of 5° and 20°.

the thickness of the TiO_2 gradient material, according to the crystallization content of the above samples. Hence, the role of the microstructure can be ignored when its depth reaches a certain value.

To evaluate the role of the slide angle and the droplet-size-unrestricted contact angle, the bouncing dynamics of droplets on samples II and IV were analyzed. As shown in Fig. 9d, when a millimetric droplet is dropped from the height of 2 cm onto the surface of sample II ((the impact velocity of 0.52 m/s), the droplet completely bounces up. The first maximum bounce is less than the initial height due to the energy loss caused by the shape change of the droplet. Then, the maximum height at the following bounces can almost remain the same. Therefore, water droplet does not further influence the surface state of the materials. This is because that TiO_2 selectively adsorbs atmospheric organic compounds while effectively repelling other adsorbates [40]. However, when the water droplet falls from the height of 10 cm onto the surface of sample II, bouncing with droplet breakup occurs with a larger impact velocity (1.4 m/s, inset "f"). It can be seen that the remainder of the droplet on the surface is not in the Wenzel state, which is removed by the fallen droplet. For sample IV (Fig. 9h), the water droplet bounces completely at the same height of 10 cm, where the time for the bounce of sample IV is smaller than sample II. The simulation of the bouncing dynamics of a droplet is shown in Fig. S6. It is found that the droplet that falls on the surface of the sample with small slip angle has less energy loss, which becomes more obvious with the increase in droplet deformation.

The bouncing dynamic of the droplet falling from the height of 10 cm onto the surface of samples II and IV with a tilt angle of 10° is shown in Fig. 9i. It can be seen that the droplet that falls onto the surface of sample II can also bounce completely. Additionally, the bouncing positions of samples II and IV are no longer in the initial falling area due to gravity. The main difference between samples II and IV, as marked by the red line, is that the bounce track of the droplet is almost perpendicular to sample IV.

Then, the specific spreading process of droplets on the surface of sample IV under different tilt conditions (5° and 20°) was investigated, and the recorded time interval of each image was 0.25 ms, as shown in Fig. 9j. It can be seen that the height in the middle of droplets is higher than both sides at the beginning of spreading, and then both ends of the droplet shrink. The position of the droplet retraction center at 2.25 ms is located at the right of its initial position. This phenomenon demonstrates that the droplet slides rapidly under the action of gravity during spreading and contracting with the surface, indicating that the friction coefficient of sample IV with the water droplet is very small.

In addition, the reflectance and wetting of the samples detected after one year showed almost the same to the one detected after three month, which meant that both the structure and material property of the samples had long-term stability.

2.3.4. Verifying that the designed micro/nano structure has the best anti-reflectance and super-hydrophobicity

In order to verify that the designed composite micro/nano structure has the best anti-reflectance and super-hydrophobicity, three kinds of other micro/nano structures with low processing efficiency and large etching amount were chosen here for comparison.

The first type of micro/nano structure was obtained by low-speed multiple scanning with a kind of laser fluence that can be used for laser-induced processing. As shown in Fig. 10 a1, the period of the microstructure is 30 μm and its surface is covered with a layer of flocculent TiO_2 nanostructures. The typical laser parameters were as follows: laser wavelength of 532 nm, single pulse energy of 2 μJ, laser repetition rate of 500 kHz, scanning interval of 30 μm, scanning mode of cross scanning, scanning speed of 30 mm/s and number of scans 5.

The second type of micro-nano structure is the micro-nano sedimentary structure [46] derived from a large amount of sediment, which is hierarchical in both vertical direction and plane. As shown in Fig. 10b1, there are several layers of structure in the vertical direction, and the uppermost layer is a dendritic micro/nano porous structure, with a minimum diameter of 2 μm and a height of 8 μm. In addition, the single tree-like microstructure also contains substructures composed of nanoparticles, which is a typical nano-tree structure. The typical laser parameters were as follows: laser wavelength of 1064 nm, single pulse energy of 200 μJ, laser repetition rate of 100 kHz, scanning interval of 50 μm, scanning mode of cross scanning, scanning speed of 5 mm/s and number of scans 1.

The third type of micro-nano structure was obtained on the basis of laser ablation structure followed by the above laser induction process. As shown in Fig. 10c1, the microstructure with a period of about 12 μm was obtained on the basis of ablation microstructure (period 50 μm), and gradient refraction material was deposited on the surface. The typical laser parameters were as follows: laser ablation with laser wavelength of 532 nm, single pulse energy of 4 μJ, laser repetition frequency of 500 kHz, scanning interval of 50 μm, scanning mode of cross scanning, scanning speed of 20 mm/s, and number of scans 4 times. The parameters of laser induction process were as follows: laser wavelength of 532 nm, single pulse energy of 12 μJ, laser repetition rate of 300 kHz, scanning interval of 5 μm, scanning mode of cross scanning, scanning speed of 30 mm/s and number of scans 1.

First, the reflectance curves of different micro-nano structures were analyzed, as shown in Fig. 10d. Among them, the designed micro/nano structure was obtained by the previous pure laser induction (Sample IV). The laser induction parameters were as follows: laser wavelength 532 nm, single pulse energy 12 μJ, laser repetition frequency 300 kHz, scanning interval 5 μm, scanning mode of cross-scanning, scanning speed 30 mm/s and number of scans 1. It can be seen from the figure that the reflectivity of samples A, B, and C is not as good as that of the previously pure induced micro-nano structure (Sample IV).

Next, the contact angle of the above micro/nano composite structure was measured after being placed in room temperature and air for three months. It can be seen that the contact angles of samples A and C are both smaller than that of the designed micro/nano structure (167°), and their slip angles are both larger than that of the designed micro/nano structure. In addition, sample B still has a superhydrophilic structure. This is because the material composition of sample B has not reached equilibrium after three months, and the high surface energy of sample B leads to hydrophilicity.

In addition, compared to the published work about the antireflective and superhydrophobic micro/nano structures using ultrashort laser-based processing, the designed structure has exhibited antireflective

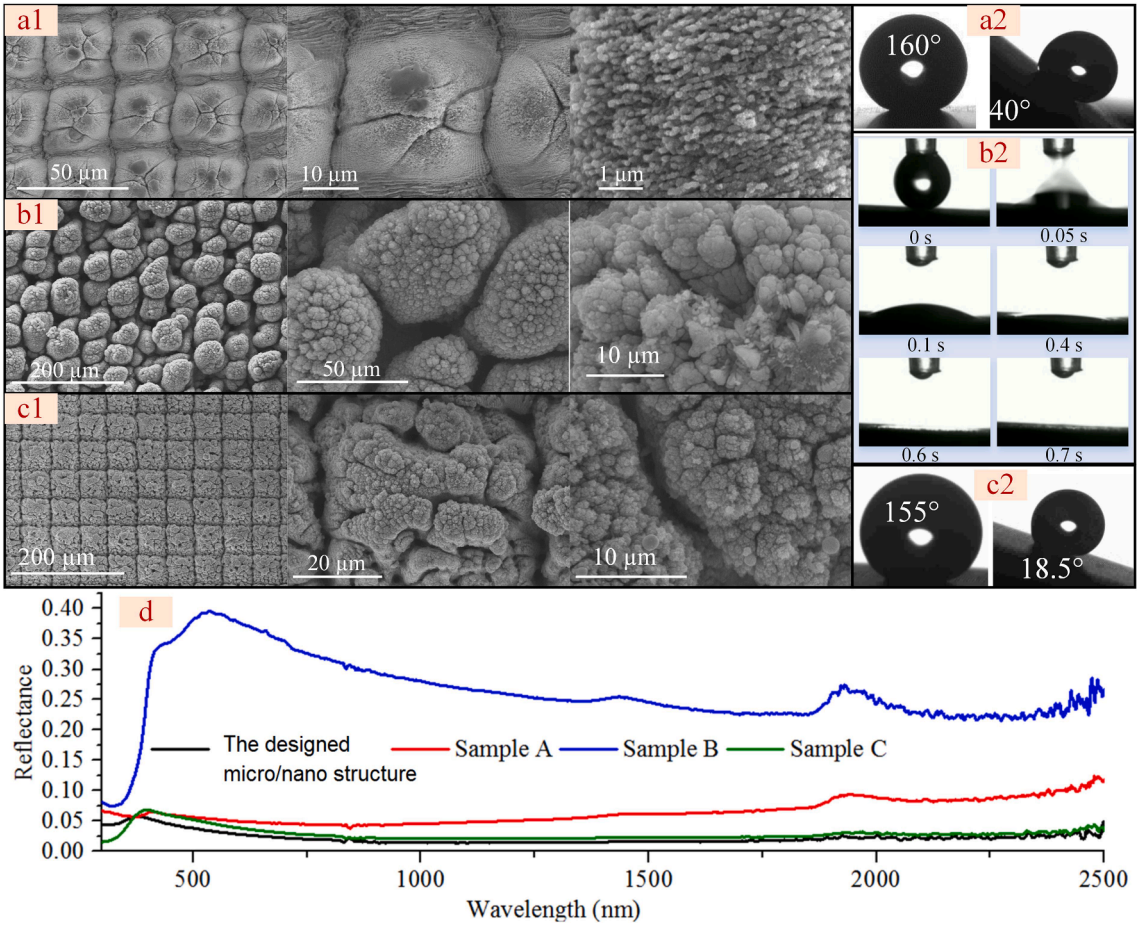

Fig. 10. (a1- c2) Three kinds of micro/nano structures and their wetting property. (d) Reflectance of the four kinds of micro/nano structures.

and superhydrophobic properties as well as a low ablated depth as shown in Table S1. Therefore, the composite micro/nano structure proposed in this paper (the period is about 12 μm, and the height of the composite micro/nano structure is about 12 μm) possesses the best anti-reflection/superhydrophobic composite functional surface. In particular, the optimal designed micro/nano structures was achieved by picosecond laser induction processing, which had the advantages of small removeal of materials, less heat accumulation effect, narrow heat affect zone and high processing efficiency. As a result, this method is applicable to crisp and hard materials, coating materials and thin-walled materials.

3. Conclusion

A new kind of composite micro/nano structure with porous nanomaterials made up of Ti gradient material and TiO_2 gradient material was proposed here. Furthermore, a new method of in-situ deposition of gradiently distributed and oxidized porous titanium nanoparticles on the surface of picosecond laser-induced micro/nano structures was presented. First, theoretical analysis shows that the porous composite layer with Ti gradient material and TiO_2 gradient material has the best anti-reflectivity. In detail, the contribution of Ti gradient material to the reduction of reflectance is mainly in the range of incident wavelength less than 10 μm, and the contribution of TiO_2 gradient material to the reduction of reflectance is mainly in the range of incident wavelength more than 10 μm. Additionally, the oxygen vacancy defects on the surface of TiO_2 can adsorb the hydrophilic –OH group and push the hydrophobic $–CH_3$ group outward to improve its superhydrophobic ability, while the air cushion effect of nanostructure endows the surface with nonadhesive superhydrophobic ability. The in-situ deposition of the porous material with a nanosecond laser verified that Ti gradient material and TiO_2 gradient material are generated at the same time. The sample full of the TiO_2 gradient porous material has the most amount of Ti gradient material, which has the lowest reflectance and shows a nonadhesive hydrophobic property. However, the nanosecond laser-induced thermal effect leads to a very small amount of Ti gradient material, limiting the antireflective performance of the sample. Then, the period and height of the composite micro/nano structure with the best super-hydrophobicity and anti-reflectivity were investigated. Theoretical work demonstrates that the period of the microstructure with excellent anti-reflection characteristics should not exceed 10 μm and the ratio of depth to width should be large. Moreover, the height of the microstructure with superhydrophobic characteristics should be greater than 10 μm and the period of the microstructure should be more than 10 μm. Therefore, the theoretical optimal microstructure period should be about 10 μm. A picosecond laser induction processing strategy is proposed for the fabrication such kind of such a composite micro/nano structure, and the designed composite micro/nano structure is obtained with only about 12 μm etched depth of the materials. It is found that the reflectance of the designed composite micro/nano structure is around 2 % from the visible band to the near-infrared band and below 20 % from the ultraviolet to middle-infrared (wavelength from 300 nm to 25 μm). In addition, the contact angle of the designed composite micro/nano structure is167 ° which is nonrestricted by the size of the droplet, and its slip angle is just 4°. Compared with other micro-nano structures that are obtained with large etching depths and low machining efficiency, the designed micro/nano structures are optimal in both anti-reflection ability and superhydrophobic characteristics.

4. Experimental section

1Preparation of the samples. A 2-mm-thick commercial pure titanium sheet (titanium content was above 99 %) was polished down to about 100 nm by an automatic polishing machine. Then, the sample was cleaned in an ultrasonic bath with acetone for 30 min and rinsed with deionized water.

Fabrication of composite micro/nano structures with picosecond pulses. The PX200-2-GF laser (EdgeWave) emits ultra-short light pulses which enter the Galvo scanning system (GalvoTech GS.9B9-10–03) through an appropriate optical path system. The focal lengths of the field lenses are 100 and 170 mm for the laser wavelengths of 532 nm and 1064 nm, respectively.

Fabrication of the deposited nanostructures with nanosecond pulses. Samples A, B, and C were processed by low-repetition nanosecond laser (InnoLas, Germany) with fixed processing parameters as follows: unfocused spot (diameter: 3.2 mm), laser wavelength of 1064 nm, repetition rate of 100 Hz, scanning interval of 200 μm, and scanning speed 0.2 mm/s. The laser power densities of samples A, B, and C were 1.40, 2.00, and 2.46 J/cm^2, respectively.

Characterization: The surface morphologies of titanium samples after laser irradiation were observed using a scanning electron microscope (Hitachi, Japan). The morphologies of microstructures and their cross sections were characterized using a laser scanning confocal microscope (Olympus OLS4000, Japan). XRD (Bruker, Germany) measurements with Cu radiation ($\lambda = 1.5406$ Å, operated at 40 kV, current 40 mA) were carried out at room temperature to determine the crystal phase composition of samples. The wettability of the surfaces was tested via an OCA20 Drop Shape Analysis System (Data physics, Germany). In detail, contact angle of a deionized water droplet (5 μL) at room temperature was obtained by applying the Laplace-Young fitting algorithm to the images recorded with a Charge Coupled Device (CCD) camera. In addition, a high-speed camera (Optronis, CP80 − 3 - M − 540) was used to monitor the bouncing dynamic of the water droplet. The surface reflectivity of samples was examined by an ultraviolet spectrophotometer (Shimadzu, Japan) to investigate the optical properties of the surface structures. Furthermore, a Bruker Tensor Fourier transform infrared (FTIR) spectroscope with an A562 type integrating sphere was used to measure the wavelength dependence of the total reflectance in the mid-infrared (MIR) region.

5. Simulation section

The reflectance values of nanostructures, microstructures, and micro/nano structures were computed via Wave Optic modulus of COMSOL MULTIPHYSIS. The optical properties of TiO_2 nanocluster and Ti gradient materials were computed via VASP (Vienna Ab-initio Simulation Package), and the adsorption and NVT ensemble relaxation of ethanol on the three kinds of rutile TiO_2 (1 1 0) surface was performed via VASP. Adsorption of H_2O with $–CH_3$ and –OH groups on the surface of TiO_2 and the fitting of Lennard-Jones potential between H_2O and $–CH_3$ were investigated via Dmol3 of Materials studio. Finally, molecular dynamic simulation of the contact angle of the droplet on TiO_2 surface with various energy constants was performed via LAMMPS (Large-scale Atomic/Molecular Massively Parallel Simulator), where TIP3P was applied to decrease the potential of H_2O, the radius of the droplet was 4 nm and simulation time was 2.5 ns with a simulation step of 1 fs.

Declaration of Competing Interest

The authors declare that they have no known competing financial interests or personal relationships that could have appeared to influence the work reported in this paper.

Data availability

Data will be made available on request.

Acknowledgment

This work was supported by the National Natural Science Foundation of China (NSFC). (51735010).

Appendix A. Supplementary data

Supplementary data to this article can be found online at https://doi.org/10.1016/j.cej.2023.141582.

References

[1] Y. Zhan, Q. Cheng, Y. Song, M. Li, Micro-nano structure functionalized perovskite optoelectronics: from structure functionalities to device applications, Adv. Funct. Mater. (2022) 2200385, https://doi.org/10.1002/adfm.202200385.

[2] U. Mehmood, F.A. Al-Sulaiman, B.S. Yilbas, B. Salhi, S. Ahmed, M.K. Hossain, Superhydrophobic surfaces with antireflection properties for solar applications: a critical review, Sol. Energy Mater. Sol. Cells 157 (2016) 604–623, https://doi.org/10.1016/j.solmat.2016.07.038.

[3] P. Fan, B. Bai, J. Long, D. Jiang, G. Jin, H. Zhang, M. Zhong, Broadband high-performance infrared antireflection nanowires facilely grown on ultrafast laser structured Cu surface, Nano Lett. 15 (2015) 5988–5994, https://doi.org/10.1021/acs.nanolett.5b02141.

[4] B. Wang, M. Liu, T. Huang, C. Zhao, Micro/nanostructures for far-field thermal emission control: an overview, ES Energy Environ. 6 (2019) 18-38. doi: 10.30919/esee8c360.

[5] A. Dostovalov, K. Bronnikov, V. Korolkov, S. Babin, E. Mitsai, A. Mironenko, M. Tutov, D. Zhang, K. Sugioka, J. Maksimovic, T. Katkus, S. Juodkazis, A. Zhizhchenko, A. Kuchmizhak, Hierarchical anti-reflective laser-induced periodic surface structures (LIPSSs) on amorphous si films for sensing applications, Nanoscale 12 (25) (2020) 13431–13441.

[6] W. Wang, L. Qi, Light management with patterned micro-and nanostructure arrays for photocatalysis, photovoltaics, and optoelectronic and optical devices, Adv. Funct. Mater. 29 (2019) 1807275, https://doi.org/10.1002/adfm.201807275.

[7] C. Hu, X. Xie, K. Ren, A facile method to prepare stearic acid-TiO_2/zinc composite coating with multipronged robustness, self-cleaning property, and corrosion resistance, J. Alloys Compd. 882 (2021), 160636, https://doi.org/10.1016/j.jallcom.2021.160636.

[8] J. Wei, B. Li, N. Tian, J. Zhang, W. Liang, J. Zhang, Scalable robust superamphiphobic coatings enabled by self-similar structure, protective micro-skeleton, and adhesive for practical anti-icing of high-voltage transmission tower, Adv. Funct. Mater. 32 (2022) 2206014, https://doi.org/10.1002/adfm.202206014.

[9] D. Zeng, Y. Li, D. Huan, H. Liu, H. Luo, Y. Cui, C. Zhu, J. Wang, Robust epoxy-modified superhydrophobic coating for aircraft anti-icing systems, Colloids Surf., A 628 (2021), 127377, https://doi.org/10.1016/j.colsurfa.2021.127377.

[10] X. Li, T. Shi, B. Li, X. Chen, C. Zhang, Z. Guo, Q. Zhang, Subtractive manufacturing of stable hierarchical micro-nano structures on AA5052 sheet with enhanced water repellence and durable corrosion resistance, Mater. Des. 183 (2019), 108152, https://doi.org/10.1016/j.matdes.2019.108152.

[11] Y. Liu, X. Cao, J. Shi, B. Shen, J. Huang, J. Hu, Z. Chen, Y. Lai, A superhydrophobic TPU/CNTs@ SiO2 coating with excellent mechanical durability and chemical stability for sustainable anti-fouling and anti-corrosion, Chem. Eng. J. 434 (2022), 134605, https://doi.org/10.1016/j.cej.2022.134605.

[12] J. Chen, J. Chen, L. Li, S. Wang, Y. Xie, Study on the self-cleaning phenomenon and anti-pollution flashover performance of micro-nanostructure superhydrophobic coating surface under a high humidity environment, Colloids Surf., A 630 (2021), 127552, https://doi.org/10.1016/j.colsurfa.2021.127552.

[13] Z. Ren, Q. Zheng, H. Wang, H. Guo, L. Miao, J. Wan, C. Xu, S. Cheng, H. Zhang, Wearable and self-cleaning hybrid energy harvesting system based on micro/nanostructured haze film, Nano Energy 67 (2020), 104243, https://doi.org/10.1016/j.nanoen.2019.104243.

[14] Y. Chen, Z. Quan, Y. Sun, D. Chi, D. Liu, L. Zhou, J. Zhang, Z. Mu, Z. Wang, B. Li, Durable and superhydrophobic aluminium alloy with microscale hierarchical structures and anti-drag function inspired by diving bell spider, Coatings 11 (2021) 1146, https://doi.org/10.3390/coatings11101146.

[15] H. Li, S. Kelly, D. Guevarra, Z. Wang, J.K. Nrskov, Analysis of the limitations in the oxygen reduction activity of transition metal oxide surfaces, Nat. Catal. 4 (2021) 463–468, https://doi.org/10.1038/s41929-021-00618-w.

[16] Y. Zeng, X. Fan, J. Chen, S. He, Z. Yi, X. Ye, Y. Yi, Preparation of composite micro/nano structure on the silicon surface by reactive ion etching: Enhanced anti-reflective and hydrophobic properties, Superlattices Microstruct. 117 (2018) 144–154, https://doi.org/10.1016/j.spmi.2018.03.035.

[17] N. Cherupurakal, M.S. Mozumder, A.-H.-I. Mourad, S. Lalwani, Recent advances in superhydrophobic polymers for antireflective self-cleaning solar panels, Renewable Sustainable Energy Rev. 151 (2021), 111538, https://doi.org/10.1016/j.rser.2021.111538.

[18] H. Wang, J. Zhuang, J. Yu, H. Qi, Y. Ma, H. Wang, Z. Guo, Fabrication of anti-reflective surface with superhydrophobicity/high oleophobicity and enhanced mechanical durability via nanosecond laser surface texturing, Materials 13 (2020) 5691, https://doi.org/10.3390/ma13245691.

[19] P. Wang, X. Yan, J. Zeng, C. Luo, C. Wang, Anti-Reflective superhydrophobic coatings with excellent durable and self-cleaning properties for solar cells, Appl. Surf. Sci. (2022), 154408, https://doi.org/10.1016/j.apsusc.2022.154408.

[20] H.K. Raut, V.A. Ganesh, A.S. Nair, S. Ramakrishna, Anti-reflective coatings: a critical, in-depth review, Energy Environ. Sci. 4 (2011) 3779–3804, https://doi.org/10.1039/C1EE01297E.

[21] S.J. Cho, T. An, Y.K. Jin, J.W. Sung, G. Lim, Superhydrophobic nanostructured silicon surfaces with controllable broadband reflectance, Chem. Commun. 47 (2011) 6108–6110, https://doi.org/10.1039/C1CC11615K.

[22] A.A. Bushunov, M.K. Tarabrin, V.A. Lazarev, Review of Surface modification technologies for mid-infrared antireflection microstructures fabrication, Laser Photonics Rev. 15 (2021) 2000202, https://doi.org/10.1002/lpor.202000202.

[23] Y.K. Lai, X.F. Gao, H.F. Zhuang, J.Y. Huang, C.J. Lin, L. Jiang, Designing superhydrophobic porous nanostructures with tunable water adhesion, Adv. Mater. 21 (37) (2009) 3799–3803, https://doi.org/10.1002/adma.200900686.

[24] Z. Dong, M. Vuckovac, W. Cui, Q. Zhou, R.H. Ras, P.A. Levkin, 3D printing of superhydrophobic objects with bulk nanostructure, Adv. Mater. 33 (2021) 2106068, https://doi.org/10.1002/adma.202106068.

[25] E.E. Perl, W.E. Mcmahon, J.E. Bowers, D.J. Friedman, Design of antireflective nanostructures and optical coatings for next-generation multijunction photovoltaic devices, Opt. Express 22 (Suppl 5) (2014) A1243, https://doi.org/10.1364/OE.22.0A1243.

[26] C.H. Chang, J.A. Dominguez-Caballero, H.J. Choi, G. Barbastathis, Nanostructured gradient-index antireflection diffractive optics, Opt. lett. 36 (2011) 2354–2356, https://doi.org/10.1364/OL.36.002354.

[27] E.M. Garcell, S.C. Singh, H. Li, B. Wang, S.A. Jalil, C. Guo, Comparative study of femtosecond laser-induced structural colorization in water and air, Nanoscale Adv. 2 (2020) 2958–2967, https://doi.org/10.1039/C9NA00804G.

[28] T. Lim, P.S. Mirabedini, K. Jung, P.A. Greaney, A.A. Martinez-Morales, High-index crystal plane of ZnO nanopyramidal structures: Stabilization, growth, and improved photocatalytic performance, Appl. Surf. Sci. 536 (2021), 147326, https://doi.org/10.1016/j.apsusc.2020.147326.

[29] X. Tian, T. Verho, R. Ras, Moving superhydrophobic surfaces toward real-world applications, Science 352 (2016) 142–143, https://doi.org/10.1126/science.aaf2073.

[30] D. Wang, Q. Sun, M.J. Hokkanen, C. Zhang, F.-Y. Lin, Q. Liu, S.-P. Zhu, T. Zhou, Q. Chang, B.o. He, Q. Zhou, L. Chen, Z. Wang, R.H.A. Ras, X.u. Deng, Design of robust superhydrophobic surfaces, Nature 582 (7810) (2020) 55–59.

[31] S. Xu, Q. Wang, N. Wang, Chemical fabrication strategies for achieving bioinspired superhydrophobic surfaces with micro and nanostructures: a review, Adv. Eng. Mater. 23 (2021) 2001083, https://doi.org/10.1002/adem.202001083.

[32] E. Velayi, R. Norouzbeigi, Annealing temperature dependent reversible wettability switching of micro/nano structured ZnO superhydrophobic surfaces, Appl. Surf. Sci. 441 (2018) 156–164, https://doi.org/10.1016/j.apsusc.2018.02.005.

[33] M.M. Hussain, A. Kunwar, M.K. Majeed, Y. Wang, A. Saleem, H. Ma, Superhydrophobic surface and lubricant-infused surface: Implementing two extremes on electrodeposited Ni TiO_2 surface to drive optimal wettability regimes for droplets' multifunctional behaviors, Adv. Eng. Mater. 23 (2021) 2100266. 10.1002/adem.202100266.

[34] Z.C. Ma, Y.L. Zhang, B. Han, Q.D. Chen, H.B. Sun, Femtosecond-laser direct writing of metallic micro/nanostructures: from fabrication strategies to future applications, Small Methods 2 (2018) 1700413, https://doi.org/10.1002/smtd.201700413.

[35] R. Pan, M. Cai, W. Liu, X. Luo, C. Chen, H. Zhang, M. Zhong, Extremely high Cassie-Baxter state stability of superhydrophobic surfaces via precisely tunable dual-scale and triple-scale micro–nano structures, J. Mater. Chem. A 7 (2019) 18050–18062, https://doi.org/10.1039/C9TA04484A.

[36] P. Fan, R. Pan, M. Zhong, Ultrafast laser enabling hierarchical structures for versatile superhydrophobicity with enhanced Cassie-Baxter stability and durability, Langmuir 35 (2019) 16693–16711, https://doi.org/10.1021/acs.langmuir.9b02986.

[37] A. Tavangar, B. Tan, K. Venkatakrishnan, Study of the formation of 3-D titania nanofibrous structure by MHz femtosecond laser in ambient air, J. Appl. Phys. 113 (2013) 1621–1639, https://doi.org/10.1063/1.4771667.

[38] L. Bai, L. He, Y. Fu, C. Chu, Z. Wei, R. Spinney, D.D. Dionysiou, Y. Liang, R. Xiao, New insight to superoxide radical-mediated degradation of pentachlorophenate: Kinetic determination and theoretical calculations, Chem. Commun. 58 (2022) 2666–2669, https://doi.org/10.1039/D1CC06834B.

[39] J. Yang, P. Zhu, F. Meng, Q. Guo, T. He, Z. Yang, W. Qu, H. Li, Charge distribution modulation and morphology controlling of copper selenide for an enhanced elemental mercury adsorption activity in flue gas, Chem. Eng. J. 442 (2022), 136145, https://doi.org/10.1016/j.cej.2022.136145.

[40] T. Chen, W. Wang, T. Tao, A. Pan, X. Mei, Broad-band ultra-low-reflectivity multiscale micro-nano structures by the combination of femtosecond laser ablation and in situ deposition, ACS Appl. Mater. Interfaces 12 (2020), https://doi.org/10.1021/acsami.0c16894.

[41] B. Cai, H. Chen, G. Xu, H. Zhao, S. Okihiro, Ultra-broadband THz antireflective coating with polymer composites, Polymers 9 (2017) 574, https://doi.org/10.3390/polym9110574.

[42] T. Zheng, C. Wu, M. Chen, Y. Zhang, P.T. Cummings, A DFT study of water adsorption on rutile TiO_2 (110) surface: the effects of surface steps, J. Chem. Phys. 145 (2016), 044702, https://doi.org/10.1063/1.4958969.

[43] J. Balajka, M.A. Hines, W.J. DeBenedetti, M. Komora, J. Pavelec, M. Schmid, U. Diebold, High-affinity adsorption leads to molecularly ordered interfaces on TiO_2 in air and solution, Science 361 (2018) 786–789, https://doi.org/10.1126/science.aat6752.

[44] S. Kato, A. Sunahara, M. Tsukamoto, Kinetic model for color-center formation in TiO_2 film using femtosecond laser irradiation, J. Vac. Sci. Technol., A 37 (2019), 031512, https://doi.org/10.1116/1.5085822.
[45] A. Pan, W. Wang, X. Mei, K. Wang, X. Yang, Rutile TiO_2 flocculent ripples with high antireflectivity and superhydrophobicity on the surface of titanium under 10 ns laser irradiation without focusing, Langmuir 33 (2017) 9530–9538, https://doi.org/10.1021/acs.langmuir.6b04664.
[46] A. Pan, W. Wang, X. Mei, G. Jiang, Three-dimensional micro-nano-hierarchical porous structures based on the deposition of the ablated material by picosecond pulses, in: Laser-based Micro-and Nanoprocessing XII, SPIE, (2018) 263-269. 10.1117/12.2289613.